

The orbital phase resolved spectroscopy of X-ray binary 4U 1822–371 with *Suzaku*

Shu Niu¹, Shu-Ping Yan¹, Shi-Jun Lei¹, Michael A. Nowak², Norbert S. Schulz² and Li Ji¹

¹ Purple Mountain Observatory, Chinese Academy of Sciences, Nanjing 210008, China; niushu@pmo.ac.cn

² MIT Kavli Institute for Astrophysics and Space Research, Cambridge, MA 02139, USA

Received 2015 April 27; accepted 2015 May 31

Abstract 4U 1822–371 is a typical edge-on eclipsing low mass X-ray binary and the prototype of accretion disk coronal sources. We report on the results of a spectral analysis over the energy range 0.5–45 keV observed by *Suzaku* in 2006. We extract spectra from five orbital phases. The spectra can be equally well described by various previously proposed models: an optically thick model described by a partially covered cutoff power law and an optically thin model described by a blackbody plus a cutoff power law. The optically thick model requires a covering fraction of about 55%, while the optically thin model requires a temperature of the central source of about 0.16 keV. The spectrum in the optically thick model also shows the previously detected cyclotron line feature at ~ 30 keV with the same *Suzaku* observation. This feature confirms the presence of a strong magnetic field. The Fe K α fluorescent line strengths as well as the detected Fe XXVI strengths are similar to previous *Chandra* and *XMM-Newton* detections in our phased spectral analysis; however, we also observe strong Fe XXVI during the eclipse, which indicates a slightly larger central corona.

Key words: accretion, accretion disks — binaries: eclipsing — line: formation — binaries: spectroscopic — X-rays: binaries

1 INTRODUCTION

4U 1822–371 is a typical edge-on eclipsing low mass X-ray binary and is thought to possess a prominent accretion disk corona (ADC; White et al. 1981). The precise position and optical identification were obtained by *HEAO 1* (Griffiths et al. 1978). The ratio of X-ray to optical luminosity of 4U 1822–371 is $L_X/L_{\text{opt}} \approx 30$, the orbital period is ~ 5.57 h (Seitzer et al. 1979), and its distance is ~ 2.5 kpc (Mason & Cordova 1982). The source lacks typical short-term variability such as the transformation from and to low/hard and high/soft states (Charles et al. 1980) in the X-ray light curve.

4U 1822–371 is an edge-on X-ray binary with eclipses observed over a broad energy band. The inclination is derived to be $i = 82.5^\circ \pm 1.5^\circ$ (Heinz & Nowak 2001). Jonker & van der Klis (2001) detected a pulse period at 0.59 s with *RXTE* data and identified the central compact star as a neutron star. The mass of the companion star has been estimated to be $\sim 0.5 M_\odot$.

Recent works by Parmar et al. (2000), Heinz & Nowak (2001), Iaria et al. (2001) and Ji et al. (2011) showed that the X-ray spectrum of 4U 1822–371 can be described equally well either by an optically thick model with partial covering or an optically thin model with a blackbody component in various observations with *ASCA*, *RXTE*,

BeppoSAX, *Chandra* and *XMM-Newton*. Line analysis in high spectral resolution data during different orbital phases produced good estimates of disk parameters and geometry. Sasano et al. (2014) found a cyclotron absorption line at ~ 33 keV by fitting the *Suzaku* data with an optically thin model indicating the presence of a strong magnetic field of $\sim 10^{12}$ G.

In this paper, we re-analyze *Suzaku* observations over the entire X-ray bandpass. We fit the spectrum with the optically thick and optically thin models in different orbital phases in order to test their orbital dependence. We also focus on the Fe lines above 6 keV because of the large effective area that *Suzaku* offers.

2 OBSERVATIONS

4U 1822–371 was observed with the *Suzaku* satellite observatory from 2006 Oct 02 10:57:12 to 2006 Oct 03 12:27:19 UT (Obs. ID: 401051010) using the X-ray Imaging Spectrometer (XIS) and Hard X-ray Detector (HXD) for a total exposure of about 92 ks. The XIS contains four sensitive imaging CCD cameras (XIS0–3), three of them are front-illuminated (FI; energy range 0.4–12 keV) devices and one is back-illuminated (BI; energy range 0.2–12 keV). XIS0 and XIS1 were operated in 1/4 window mode (2.0 s per frame), while XIS2 and XIS3 were

operated in full window mode (8.0 s per frame). The HXD sensors are composed of a Positive Intrinsic Negative (PIN, with an energy range of 10–70 keV and 61 μ s per frame) detector and a Gadolinium Silicate (GSO, with an energy range of 40–600 keV and 61 μ s per frame) detector.

We reprocess all the observational data using HeaSoft Version 6.16 with the most recent CALDB files. We then analyze the products using ISIS 1.6.2¹.

3 DATA REDUCTION

3.1 Light Curve

After standard screening criteria were applied as well as the barycenter correction, we obtain an exposure time of about 33.9 ks in the XIS. We extract the events in all four XIS fields of view from the same annulus region with an inner radius of 30'' and an outer radius of 260''. The size of the inner radius mitigates event pileup to be less than 5% in every CCD chip with an average of $\leq 3\%$ estimated by *aeattcor* and *pile_estimate* scripts² in ISIS, and the outer radius which encircles 99% of the point source flux as referred to from the *Suzaku* ABC guide³. We extract the backgrounds from regions around this annulus.

In the GSO band we extract the light curve from 50 to 300 keV and find that the count rate (~ 0.4 cts s^{-1}) is quite low with respect to the background (> 20 cts s^{-1}). This leads to systematic uncertainties that may be a significant issue for the light curve in the very hard X-ray band. Similarly, we find that 4U 1822–371 is also very dim with respect to the background uncertainties in the spectrum of the entire GSO energy bandpass and therefore decided to discard the GSO data in the spectral analysis.

3.2 Energy Band Selection of the Spectra

For XIS, we ignore the data in 5×5 edit mode because the exposure time of this mode is very short, leading to poor statistics for its spectra. We extract the spectrum in the 3×3 mode and notice the energy in the 0.5–12.0 keV band which has a high effective area.

PIN is unable to image the source. We just reprocess the data with standard procedures and use the response files and background files from the database archives provided by the *Suzaku* team. Figure 1 shows the PIN spectra in the 15–70 keV band: data-background (net data), background and 3% background. We find that the 3% background is higher than the net data above 45 keV and we thus limit the energy range to 15–45 keV.

3.3 Pileup

Pileup⁴ has to be taken into account, especially when the central source is bright. Pileup occurs in CCD detectors when two or more photons fall on the same pixel during one frame time, and are recorded as a single event with the combined photon energies. The spectrum therefore shifts towards higher energies.

A common method to mitigate pileup is to select the source region excluding the innermost region where pileup is severe. Another correction method is to fit the piled-up spectrum following a model procedure by Davis (2001). In order to minimize the effect of pileup, we first run the *aeattcor* script to improve the attitude correction of every XIS CCD image after standard calibration and screening steps. Then we extract spectra from an annulus in order to obtain a (relatively) pileup free spectrum. Finally one can estimate the relevant pileup parameters from the model of Davis (2001) (e.g., frame time, number of regions and PSF fraction to apply to the pileup model) for the remaining annulus region. In this way, the *pile_estimate* script estimates that the pileup fractions of four CCD annuluses are less than 5%. Note, all the spectral fitting in the following sections has been done with and without a pileup kernel. In both cases, the parameters we obtained are almost identical. Therefore, we only present our results without a pileup kernel. All the uncertainties in this paper are given at the 90% confidence level (c.l.).

4 DATA ANALYSIS AND DISCUSSION

4.1 Light Curve

In the previous work by Iaria et al. (2011), the ephemeris of 4U 1822–371 was described by a quadratic function

$$T_{\text{ecl}} = 45614.80954(14)\text{MJD}_{\odot} + 0.2321088628(21)N + 1.648(72) \times 10^{-11}N^2. \quad (1)$$

The time unit is in barycentric Modified Julian Date (MJD_{\odot}) and N is the cycle number. This leads to an orbital period of $P_{\text{orb}} \sim 5.57$ h with a very small \dot{P}_{orb} .

Figure 2 shows the unfolded light curve obtained from the combined data from the CCDs in XIS. The black plus symbols are the data resulting from the 3×3 mode and the grey ones are those from the 5×5 mode. The gaps in the light curve are due to the occultation of *Suzaku* by the Earth. Because the total exposure time is less than two full orbital periods, we cannot obtain an accurate enough period from the power spectral density method or other statistical methods such as those in Davies (1990) alone. So, we fold the light curve into 500 bins with the latest obtained period (Iaria et al. 2011). We note that the XIS light curve does not show an obvious broad dip before the eclipse as was observed in the *Chandra* High

¹ <http://space.mit.edu/CXC/ISIS/>

² <http://space.mit.edu/CXC/software/suzaku/index.html>

³ <http://heasarc.gsfc.nasa.gov/docs/suzaku/analysis/abc/>

⁴ http://cxc.harvard.edu/ciao/ahelp/acis_pileup.html

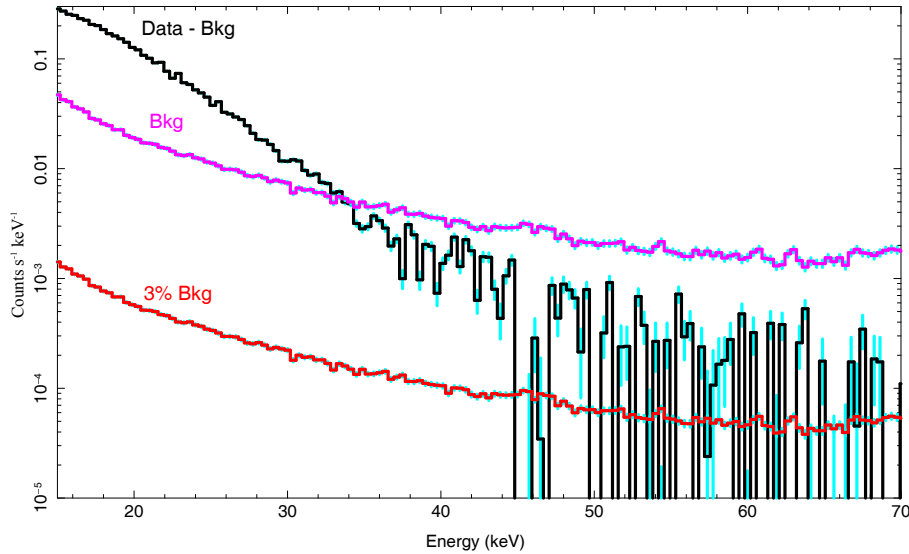


Fig. 1 The PIN spectrum: data-background (*black line*), background (*magenta line*) and 3% background (*red line*) are plotted. The source could be significantly affected by uncertainties in the background above 45 keV.

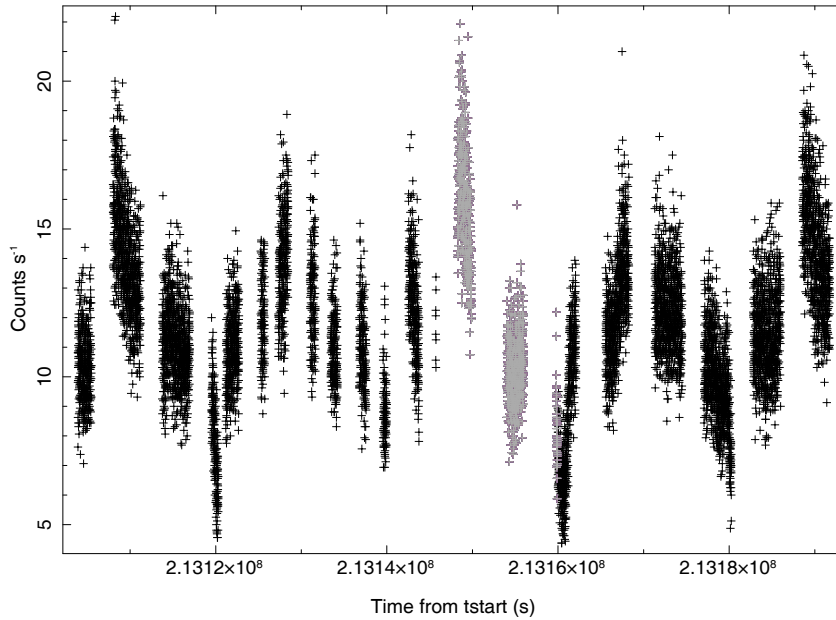


Fig. 2 Unfolded light curves of 4U 1822–371 which are combined with data from four CCDs in XISs data. The black plus symbols are the data resulting from the 3×3 mode and the grey ones are those from the 5×5 mode.

Energy Transmission Grating (HETG) data (Ji et al. 2011). Previous observations (White et al. 1981; Jain et al. 2010; Iaria et al. 2013) showed that the phase-folded light curve profiles of 4U 1822–371 can slightly change with time; therefore, rather than determining the time of zero orbital phase by a fit to the entire folded light curve, we instead determine the time of this phase via fits to portions of the light curve very near the eclipse. We use a Gaussian and a linear component to fit the phase (Parmar et al. 2000) around the eclipse. The corresponding JD_{\odot} of the best fit eclipse time is $2454011.17295^{+0.00024}_{-0.00031}$, which is consistent with the value obtained by Iaria et al. (2011).

The difference in the eclipse time Δt is about 5 s, less than the time resolution. The black solid line in Figure 3 shows the folded XIS light curve. The exposure time of the HXD is about 31 ks. We extract the light curve for the 15–60 keV band, which has relatively low background uncertainties, and fold it using the same parameters as for the folded XIS light curve. The scaled red dashed line in Figure 3 denotes the PIN light curve. The profile of the PIN light curve is very similar to the softer X-ray band of the XIS. However, we find that the peak of the PIN light curve is broader than that in the XIS light curve, and we see some other minor deviations. More interesting, the peak of

the PIN light curve precedes that of the XIS light curve by about 900 s, which further supports the idea that the soft X-ray emission mainly comes from the hot spot.

The hot spot scenario was first suggested by Mason et al. (1980) and further confirmed by *Chandra* data (Cottam et al. 2001; Ji et al. 2011). The schematic illustration of this system was given by Cottam et al. (2001) and Iaria et al. (2013) based on *Chandra* and *XMM-Newton* observations. Although the *Suzaku* light curve is not exactly the same as those from *Chandra* (Ji et al. 2011) and *XMM-Newton* (Iaria et al. 2013), Jain et al. (2010) showed that the light curves of 4U 1822–371 during different orbital cycles have different profiles, especially during phases before and after eclipses. So, we can give a modified illustration. We think that the disappearance of the broad dip before an eclipse occurs is caused by shifts in the position of the point of impact on the accretion stream or the accretion material is not transferred steadily.

4.2 Broadband Spectrum

First we obtain the overall physical properties of the broadband spectrum of 4U 1822–371. Because the central source is obstructed by the central corona at a high inclination angle, the photons from the inner region will be reprocessed by an optically thick corona. The atmosphere above the disk beyond the radius of this corona will partially cover the emission from the corona. Thus, we use a model consisting of a cutoff power law (*cutoffpl*), a partial covering fraction absorption (*pcfabs*), and an interstellar absorption model (*tbnew*) to fit the overall continuum. The cross-normalization between XIS and PIN is fixed at 1.16⁵. We add two Gaussian lines at the energies 6.4 and 6.9 keV to account for significant residuals in the iron line range. The interstellar medium absorption model adopts abundances from Wilms et al. (2000) and the photoelectric cross-sections from Verner et al. (1996). A cyclotron absorption line (*cyclabs*) caused by an electron rotating in a strong magnetic field, as reported by Sasano et al. (2014), is also required.

The final continuum model then reads *tbnew* * *pcfabs* * (*cutoffpl* + *gaussian1* + *gaussian2*) * *cyclabs* and gives a good fit to the spectrum with a reduced χ^2 of 1.25. Figure 4 shows the overall spectra for the XIS and PIN. The cyclotron line energy (~ 30 keV) is fairly consistent with the value obtained by Sasano et al. (2014). The magnetic field strength (Jonker & van der Klis 2001) can be estimated to be about 10^{12} G. The Si XIV Ly α and Ne IX triplet are not resolved by *Suzaku* but appear as small humps around 0.9 and 2.0 keV in the residuals. The low count rate at the high energy tail of the PIN causes some of the remaining residuals. Table 1 gives the best fit parameters of the overall spectrum of the observation for this optically thick model.

Table 1 Fitting Parameters of the Broadband Spectrum with the Partial Covering Model

Parameter	Value
N_{H} (10^{20} cm $^{-2}$)	$1.69^{+1.73}_{-1.38}$
f_{pc}	$0.46^{+0.02}_{-0.02}$
N_{Hpc} (10^{22} cm $^{-2}$)	$5.91^{+0.20}_{-0.22}$
N_{cpl} (10^{-2})	$3.08^{+0.17}_{-0.16}$
Γ_{cpl}	$0.52^{+0.11}_{-0.08}$
E_{cpl} (keV)	$13.00^{+11.87}_{-2.45}$
E_{cycl} (keV)	$29.40^{+3.63}_{-7.47}$
W_{cycl} (keV)	$27.15^{+45.83}_{-10.83}$
D_{cycl}	$0.91^{+0.20}_{-0.20}$
N_{gauss1} (10^{-3})	$0.45^{+0.04}_{-0.03}$
E_{gauss1} (keV)	$6.397^{+0.007}_{-0.007}$
σ_{gauss1} (keV)	$0.062^{+0.013}_{-0.013}$
N_{gauss2} (10^{-3})	$0.33^{+0.04}_{-0.04}$
E_{gauss2} (keV)	$6.910^{+0.026}_{-0.026}$
σ_{gauss2} (keV)	$0.168^{+0.029}_{-0.029}$
χ^2_{red} (d.o.f)	1.25(1618)

Notes: The errors associated with each parameter are at the 90% c.l.

Adopting the distance to 4U 1822–371 of 2.5 kpc estimated by Mason & Cordova (1982), we can determine the unabsorbed luminosity in the 0.5–10 keV band to be 4.3×10^{35} erg s $^{-1}$ and in the 0.5–50 keV band to be 1.4×10^{36} erg s $^{-1}$, in agreement with the results from Iaria et al. (2013) and Sasano et al. (2014).

To compare our analysis with the one by Sasano et al. (2014), we fit the broadband data with the optically thin model consisting of a blackbody plus a cutoff power law. The parameters of the best fit are very similar to the results of Sasano et al. (2014), but the reduced χ^2 of the best fit is worse. This is probably due to the wider energy range applied during the fitting and the lower number of free parameters.

4.3 Phased Spectra and Iron Emission Lines

In order to compare the properties of the iron K α line emission with previous findings, we divide our data into five phase segments as shown in Figure 3. We select the five phases from 0.045–0.18 (phase 1), 0.18–0.34 (phase 2), 0.34–0.52 (phase 3), 0.52–0.96 (phase 4) and 0.96–1.045 (phase 5). Due to the relatively low energy resolution and the low count rate of PIN, we only use the XIS data in this section.

We fit the five phases with the optically thick model. We fix the interstellar absorption column density at the best fit parameter of the unphased spectrum. Phase 5 contains the eclipse and has a low count rate above 10 keV; here we limit the energy range to 10 keV, while in the other phases we fit the 0.5 to 12 keV band. The best fit parameters are listed in Table 2. The reduced χ^2 (dof) of the five phases are 1.07 (1577), 1.08 (1577), 1.06 (1577), 1.10 (1577) and

⁵ <http://heasarc.gsfc.nasa.gov/docs/suzaku/analysis/watchout.html>

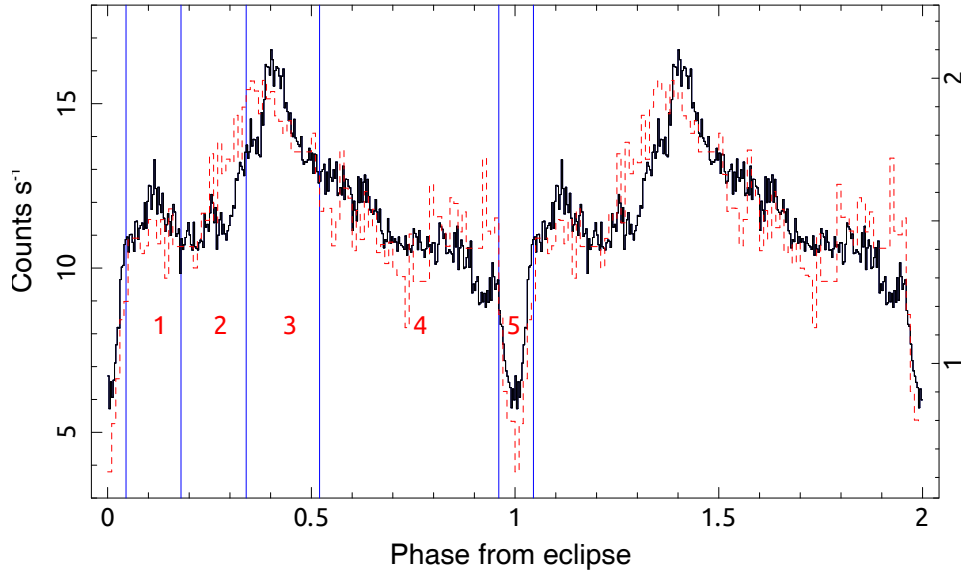


Fig. 3 Black solid line: XIS light curve folded into 500 bins. Red dashed line: PIN light curve folded into 200 bins. The PIN count rate is scaled to the mean count rate of XIS. A phase of 0 is defined by the time of the eclipse in the observation. The lines and red numbers divide one period into five phases: 0.045–0.18 (phase 1), 0.18–0.34 (phase 2), 0.34–0.52 (phase 3), 0.52–0.96 (phase 4) and 0.96–1.045 (phase 5).

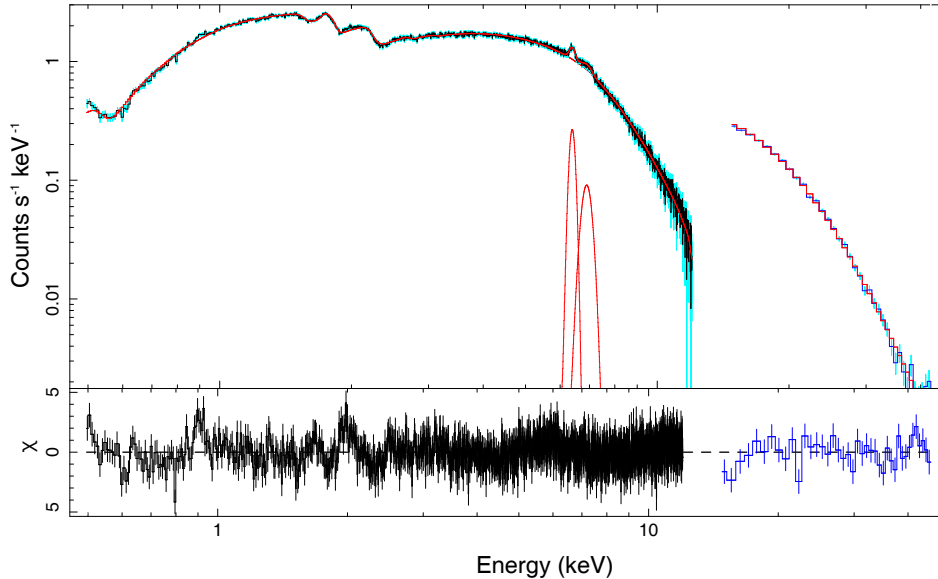


Fig. 4 The broadband spectra of XIS (*black*) and PIN (*blue*) for 4U 1822–371. It is fitted in ISIS in the pileup kernel with the model: $\text{tbnew} * \text{pcfabs} * (\text{cutoffpl} + \text{gaussian1} + \text{gaussian2}) * \text{cyclabs}$. The continuum and line components in red lines are plotted individually. The fitting parameters are shown in Table 1.

1.00 (1303), respectively. We also fit the phased spectra with the optically thin model.

The spectra of the five phase segments are shown in Figure 5. The middle and bottom panels of every phase are the residuals using the partial covering model and the blackbody plus cutoff power law model. Table 3 displays the best fit parameters of the five phases. The reduced χ^2

values are comparable for the two models, ranging between 1.00–1.10. The blackbody temperatures of the optically thin model are about 0.16 keV during different phases, which is consistent with the overall spectral value in Sasano et al. (2014) and the value obtained with *Chandra* (Ji et al. 2011). This is consistent with the scenario that the central source does not vary with phase in the optically

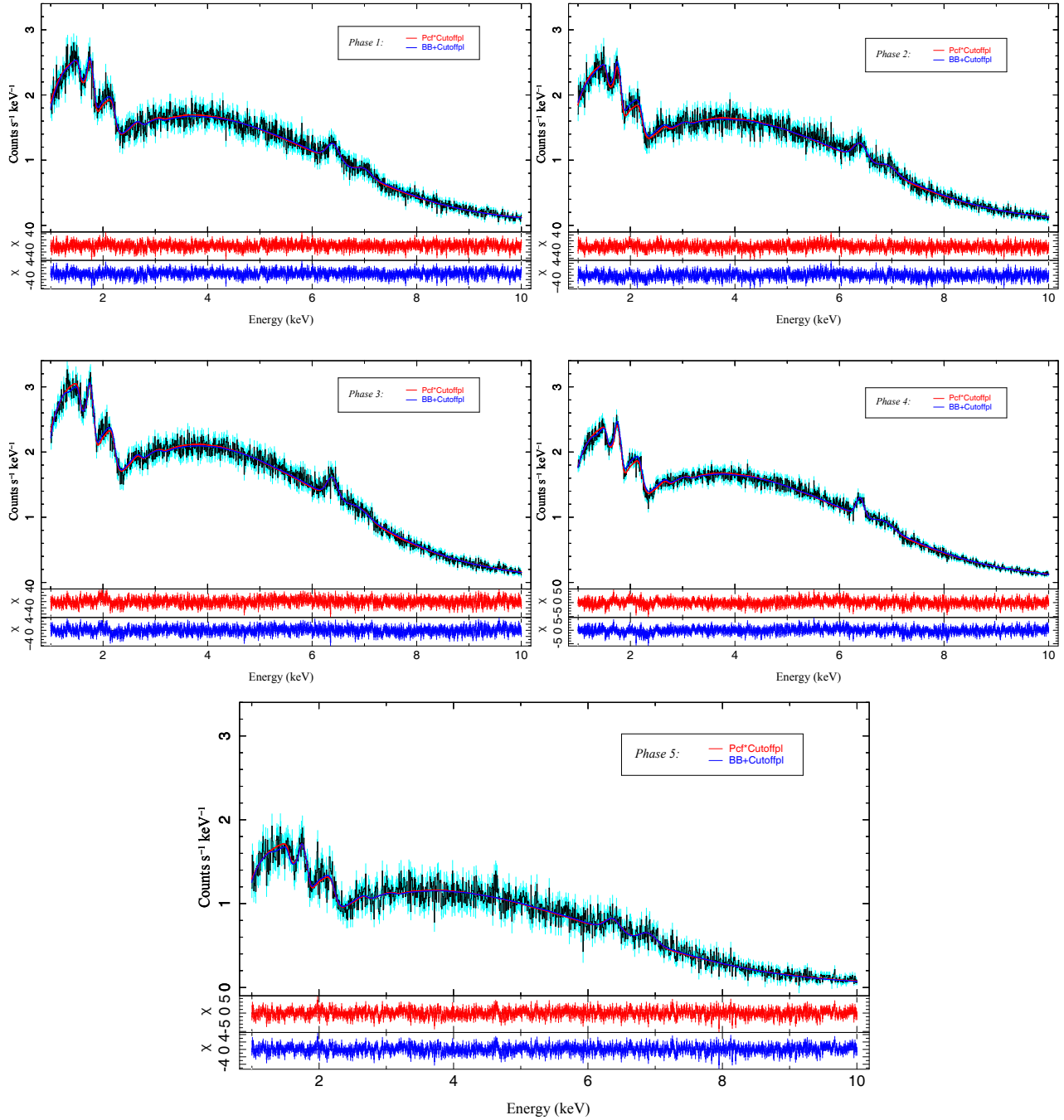


Fig. 5 The XIS spectra of the five phases. From the top left to the bottom center is from phase 1 to 5. The middle and bottom panels of each image are the 1–10 keV residuals of partial covering and blackbody plus cutoff power law models. These two models have similar goodness of fits. The fitting parameters are shown in Tables 2 and 3.

thin model. However, note that observations by *BeppoSAX* (Parmar et al. 2000) and *ASCA* (Heinz & Nowak 2001) exhibited higher temperatures of 1.3–1.8 keV.

In Figure 6, we plot some other important parameters of different phases to compare the variations of these two models. The black circles are the parameters corresponding to partial covering and the red triangles are those of blackbody plus cutoff power law.

Note that although the two models have similar qualities, the photon indices and cutoff energies are significantly different. The optically thick model has a $\Gamma \sim 0.7$ and a cutoff energy ~ 16 keV. The optically thin model has an even harder spectral slope, $\Gamma \sim 0.0$, and a lower cutoff energy, ~ 6 keV. These two different cutoff power laws have already been reported by Heinz & Nowak (2001) with *ASCA* and *RXTE* data. Sasano et al. (2014) discussed the

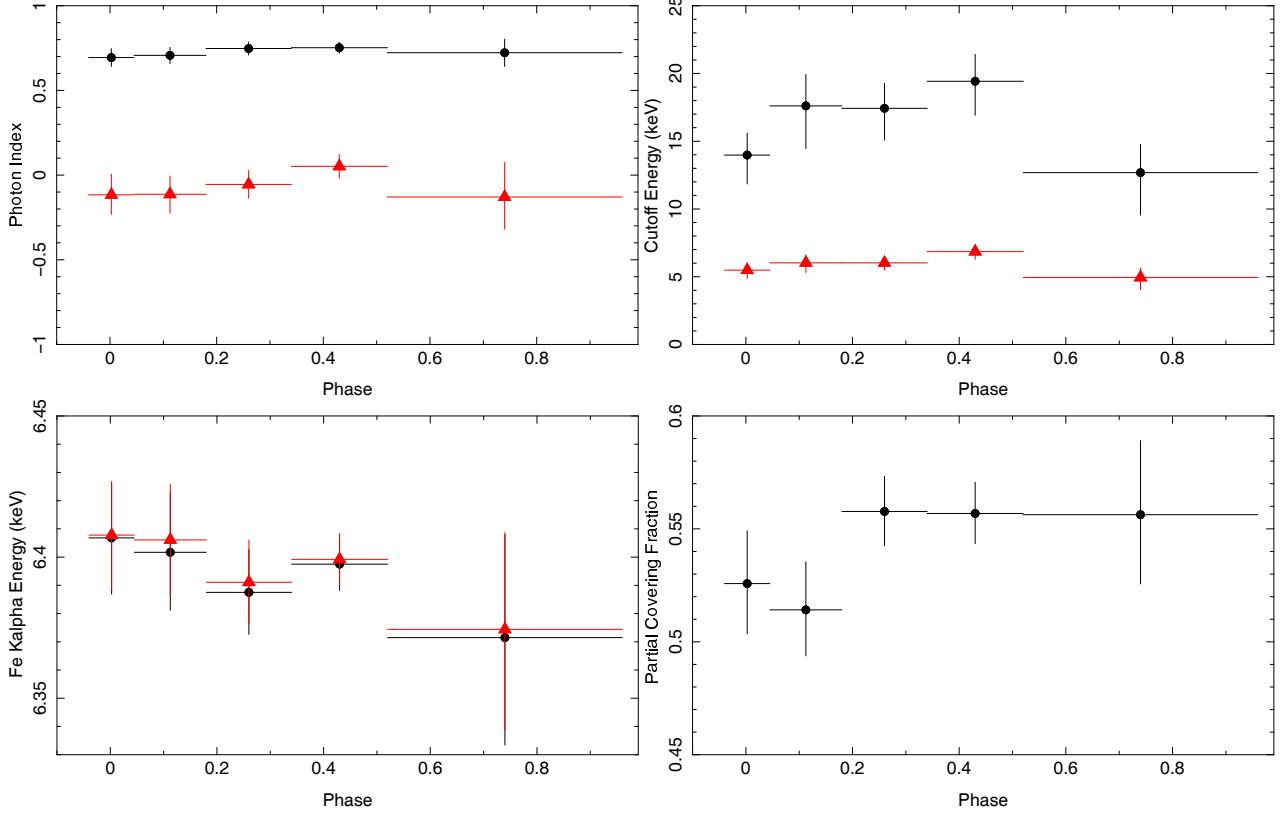


Fig. 6 Comparison of the fitting parameters between the two models during different phases: Photon Index, Cutoff Energy, Fe $K\alpha$ line energy, and partial covering fraction. The circles are the parameters of partial covering and the triangles are those of blackbody plus cutoff power law. The fitting parameters are shown in Tables 2 and 3.

Table 2 Fitting Parameters of Five Phases with the Partial Covering Model

Phase	N_{H} (10^{20} cm^{-2})	f_{pc}	$N_{\text{H}_{\text{pc}}}$ (10^{22} cm^{-2})	N_{cpl} (10^{-2})	Γ_{cpl}	E_{cpl} (keV)	N_{gauss1} (10^{-4})	E_{gauss1} (keV)	σ_{gauss1} (keV)	N_{gauss2} (10^{-4})	E_{gauss2} (keV)	σ_{gauss2} (keV)
1 (0.045–0.18)	1.69 (fixed)	$0.526^{+0.022}_{-0.023}$	$6.37^{+0.41}_{-0.37}$	$3.66^{+0.18}_{-0.17}$	$0.69^{+0.05}_{-0.05}$	$13.98^{+2.13}_{-1.63}$	$5.39^{+0.86}_{-0.80}$	$6.407^{+0.020}_{-0.019}$	$0.102^{+0.031}_{-0.028}$	$2.83^{+0.87}_{-0.78}$	$7.013^{+0.047}_{-0.059}$	$0.128^{+0.063}_{-0.054}$
2 (0.18–0.34)	—	$0.514^{+0.020}_{-0.021}$	$6.97^{+0.45}_{-0.40}$	$3.46^{+0.15}_{-0.15}$	$0.71^{+0.05}_{-0.05}$	$17.61^{+3.15}_{-2.32}$	$5.49^{+1.11}_{-0.95}$	$6.402^{+0.021}_{-0.021}$	$0.108^{+0.047}_{-0.035}$	$3.66^{+1.04}_{-0.90}$	$6.956^{+0.050}_{-0.060}$	$0.163^{+0.069}_{-0.055}$
3 (0.34–0.52)	—	$0.558^{+0.015}_{-0.015}$	$6.77^{+0.28}_{-0.27}$	$4.84^{+0.17}_{-0.17}$	$0.75^{+0.04}_{-0.04}$	$17.43^{+2.35}_{-1.84}$	$5.85^{+0.70}_{-0.66}$	$6.388^{+0.015}_{-0.015}$	$0.079^{+0.050}_{-0.034}$	$4.50^{+0.39}_{-0.42}$	$6.914^{+0.165}_{-0.200}$	$0.217^{+0.271}_{-0.277}$
4 (0.52–0.96)	—	$0.557^{+0.013}_{-0.014}$	$6.05^{+0.20}_{-0.19}$	$3.67^{+0.11}_{-0.10}$	$0.75^{+0.03}_{-0.03}$	$19.43^{+2.51}_{-1.99}$	$3.77^{+0.44}_{-0.47}$	$6.397^{+0.009}_{-0.009}$	$0.032^{+0.021}_{-0.032}$	$3.49^{+0.68}_{-0.58}$	$6.873^{+0.039}_{-0.048}$	$0.177^{+0.051}_{-0.035}$
5 (0.96–1.045)	—	$0.556^{+0.031}_{-0.033}$	$6.37^{+0.58}_{-0.51}$	$2.70^{+0.19}_{-0.18}$	$0.72^{+0.08}_{-0.08}$	$12.68^{+3.12}_{-2.09}$	$2.87^{+1.06}_{-0.86}$	$6.372^{+0.038}_{-0.037}$	$0.096^{+0.085}_{-0.073}$	$2.56^{+0.95}_{-0.77}$	$6.903^{+0.041}_{-0.055}$	$0.100^{+0.083}_{-0.063}$

Notes: The errors associated with each parameter are at the 90% c.l.

power law index and cutoff energy of 4U 1822–371 with other LMXBs and showed that 4U 1822–371 was more similar to accreting pulsars than to hard-state LMXBs. In our partial covering model, the cutoff energy and photon index are more comparable to the majority of accreting pulsars.

The partial covering parameters do not vary significantly during the different phases. This might be expected if we observed isotropic circumbinary absorption. The value is consistent with the results from observations by *ASCA* (Heinz & Nowak 2001), *Chandra* (Ji et al. 2011;

Iaria et al. 2013) and *XMM-Newton* (Iaria et al. 2013). The column density of the intrinsic absorption is two magnitudes higher than the interstellar column. The photon indices of the cutoff power law are about 0.7 during all phases and flux variations are mainly caused by the continuum. The 0.5–10 keV unabsorbed flux of phase 3 is the highest at $8.16 \times 10^{-10} \text{ erg cm}^{-2} \text{ s}^{-1}$. The fluxes of phases 1, 2, 4 and 5 are about 76%, 76%, 78% and 52% that of phase 3, respectively. The values are consistent with *XMM-Newton* data (Iaria et al. 2013).

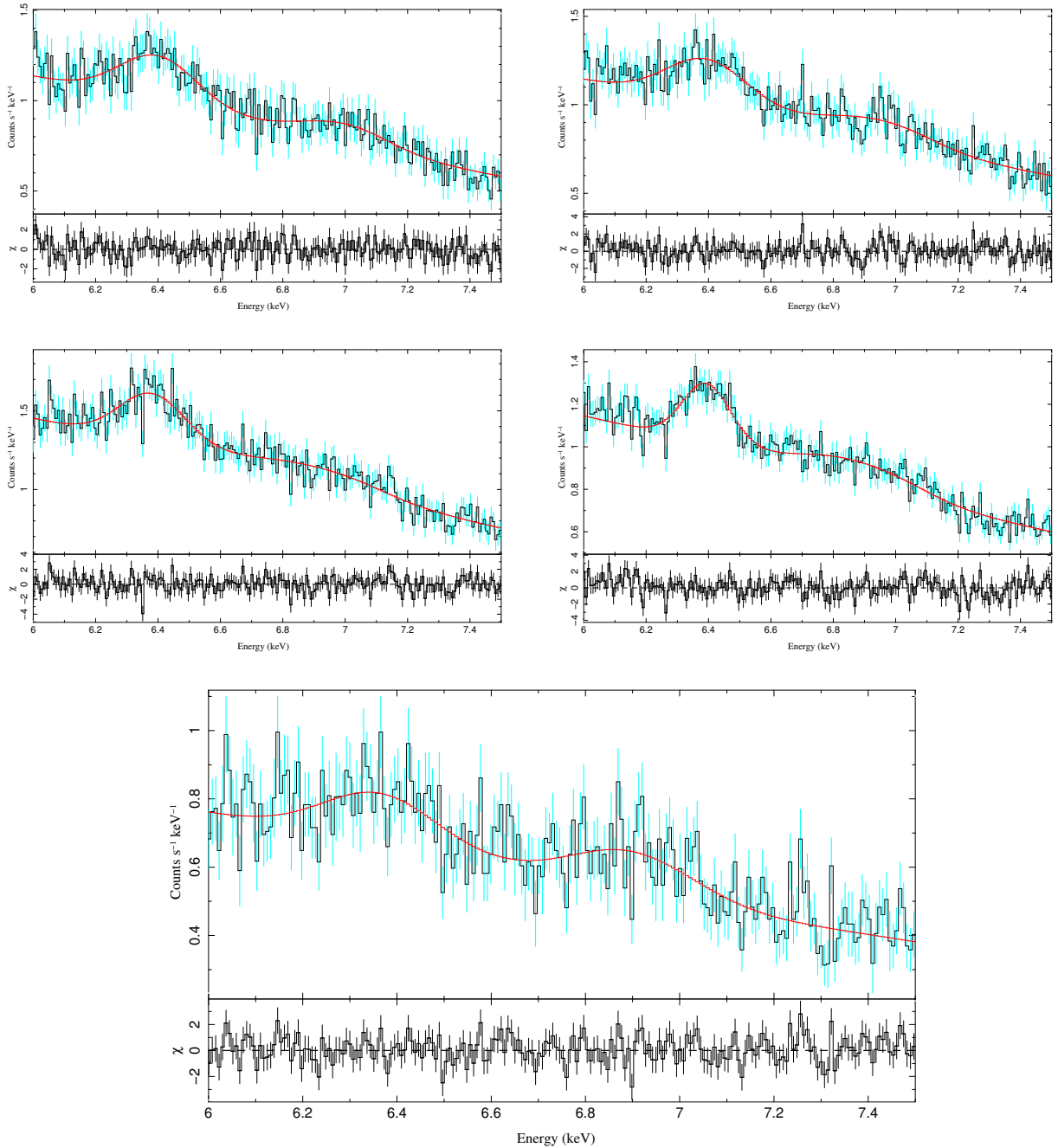


Fig. 7 The spectrum of iron lines during five phases. From the top left to the bottom center is from phase 1 to 5. The Fe $K\alpha$ line is prominent during all the phases. The fitting parameters are shown in Tables 2 and 3.

Figure 7 shows the spectrum in the iron $K\alpha$ line regions for the five phases. Like the data of *Chandra* (Ji et al. 2011) and *XMM-Newton* (Iaria et al. 2013), the addition of the Gaussian Fe XXVI line yields a good improvement to the fit statistic in this range.

The Fe $K\alpha$ lines can be detected during all the observations of *Suzaku*. Fe $K\alpha$ is produced in the corona at a distance from the central neutron star of less than $\sim 3 \times 10^{10}$ cm as described by Ji et al. (2011) and Iaria

et al. (2013). The flux of this line during the eclipse is lowest and is about half of the maximum. The flux ratio of this line during eclipse versus maximum is larger than the one for *Chandra* and *XMM-Newton* from the observations (Ji et al. 2011; Iaria et al. 2013), but is close to that in *ASCA* observations (Heinz & Nowak 2001). We think it is due to the dividing method and widths of the selected phases.

We detect a strong Fe XXVI line during the eclipse (see Table 2 and 3), which indicates a slightly larger cen-

Table 3 Fitting Parameters of Five Phases with Blackbody Plus Cutoff Power Law

Phase	N_{H} (10^{22} cm $^{-2}$)	N_{bb} (10^{-2})	T_{bb} (keV)	N_{cpl} (10^{-2})	Γ_{cpl}	E_{Cpl} (keV)	N_{gauss1} (10^{-4})	E_{gauss1} (keV)	σ_{gauss1} (keV)	N_{gauss2} (10^{-4})	E_{gauss2} (keV)	σ_{gauss2} (keV)
1 (0.045–0.18)	$0.32^{+0.25}_{-0.28}$	$0.043^{+0.047}_{-0.028}$	$0.18^{+0.02}_{-0.02}$	$1.62^{+0.17}_{-0.16}$	$-0.12^{+0.12}_{-0.12}$	$5.49^{+0.62}_{-0.52}$	$4.63^{+0.78}_{-0.73}$	$6.408^{+0.020}_{-0.019}$	$0.090^{+0.030}_{-0.029}$	$2.02^{+0.77}_{-0.70}$	$7.005^{+0.048}_{-0.065}$	$0.096^{+0.068}_{-0.083}$
2 (0.18–0.34)	$0.15^{+0.24}_{-0.15}$	$0.033^{+0.034}_{-0.017}$	$0.16^{+0.02}_{-0.04}$	$1.48^{+0.15}_{-0.12}$	$-0.11^{+0.11}_{-0.11}$	$6.03^{+0.72}_{-0.58}$	$4.89^{+0.94}_{-0.81}$	$6.406^{+0.020}_{-0.020}$	$0.099^{+0.042}_{-0.033}$	$2.81^{+0.84}_{-0.75}$	$6.935^{+0.048}_{-0.058}$	$0.131^{+0.061}_{-0.055}$
3 (0.34–0.52)	$0.57^{+0.17}_{-0.18}$	$0.132^{+0.078}_{-0.051}$	$0.16^{+0.01}_{-0.01}$	$2.13^{+0.15}_{-0.15}$	$-0.06^{+0.08}_{-0.08}$	$6.02^{+0.52}_{-0.45}$	$5.28^{+0.78}_{-0.85}$	$6.391^{+0.015}_{-0.015}$	$0.072^{+0.024}_{-0.024}$	$3.22^{+1.00}_{-0.82}$	$6.888^{+0.063}_{-0.044}$	$0.175^{+0.074}_{-0.047}$
4 (0.52–0.96)	$0.56^{+0.14}_{-0.14}$	$0.123^{+0.051}_{-0.038}$	$0.15^{+0.01}_{-0.01}$	$1.79^{+0.11}_{-0.10}$	$0.05^{+0.07}_{-0.07}$	$6.85^{+0.57}_{-0.49}$	$3.50^{+0.39}_{-0.39}$	$6.399^{+0.009}_{-0.009}$	$0.027^{+0.022}_{-0.027}$	$2.82^{+0.55}_{-0.50}$	$6.865^{+0.039}_{-0.046}$	$0.155^{+0.039}_{-0.031}$
5 (0.96–1.045)	$0.54^{+0.36}_{-0.41}$	$0.071^{+0.060}_{-0.050}$	$0.16^{+0.02}_{-0.01}$	$1.19^{+0.02}_{-0.02}$	$-0.13^{+0.19}_{-0.20}$	$4.95^{+0.92}_{-0.70}$	$2.47^{+0.97}_{-0.74}$	$6.374^{+0.036}_{-0.034}$	$0.079^{+0.081}_{-0.79}$	$2.31^{+0.83}_{-0.70}$	$6.901^{+0.040}_{-0.054}$	$0.089^{+0.072}_{-0.063}$

Notes: The errors associated with each parameter are at the 90% c.l.

tral corona. The lowest flux of the Fe XXVI line during the eclipse is about 60% of the maximum. This line has not been detected during the eclipse with a *Chandra* HETG observation or with other H-like or He-like lines (Ji et al. 2011). The large effective area of *Suzaku* helps us to resolve it. The equivalent widths of Fe K α and Fe XXVI lines do not vary much with phases. The ratios of equivalent widths of minimum versus maximum are about 60%, which are consistent with Heinz & Nowak (2001) and Iaria et al. (2013).

We find that the line center of Fe K α does not shift significantly from the expected value for low ionizations (Fe I - X) except during the eclipse (phase 5). The value of Fe K α during the eclipse is red-shifted to 6.372 ± 0.037 keV, which has also been detected in Iaria et al. (2013), indicating a velocity of ~ 1000 km s $^{-1}$. However, we note that the error bar is larger than those during other phases (see Fig. 6). This could be due to random noise or a systematic effect.

5 CONCLUSIONS

We analyze the *Suzaku* observation of the typical ADC source 4U 1822–371. The results we obtained are as follows:

- The light curve of 4U 1822–371 has a slightly different profile in different energy ranges. The peak of the PIN light curve precedes that of the XIS light curve by about 900 s, which suggests that the soft X-ray emission mainly comes from the hot spot.
- The overall spectra of the *Suzaku* observation can be fitted equally well in the broadband range: 0.5–45 keV by an ‘optically thick’ or ‘optically thin’ corona model. The optically thick model gives a $\sim 55\%$ partial covering by absorption material in all phases, while the optically thin model shows a stable radiation temperature from the central source. This similar fitting result has been presented in previous work. However, the different power law parameters are the indicators of the central compact region which we will aim to resolve with future missions. More data from a higher or

lower energy range can help us to differentiate these two models.

- The spectra also show the previously detected cyclotron line feature at ~ 30 keV which confirms the presence of a strong magnetic field of about 10^{12} G. However, the other cyclotron parameters, such as depth and width, are different from the previous detection by Sasano et al. (2014), which indicate that the properties of the magnetic field in the two models are not the same. Further observations by *Nustar* are needed to distinguish them.
- The Fe K α fluorescent line strengths as well as the detected Fe XXVI strengths are similar to previous *Chandra* and *XMM-Newton* detections; however, we also observe strong Fe XXVI during the eclipse, which indicates a slightly larger central corona.

Acknowledgements This work is supported by the National Natural Science Foundation of China (Grant No. 11273062). L. Ji is also supported by the 100 talents program of the Chinese Academy of Sciences. We also would like to thank the anonymous referee for his/her useful suggestions.

References

- Charles, P., Barr, P., & Thorstensen, J. R. 1980, *ApJ*, 241, 1148
- Cottam, J., Sako, M., Kahn, S. M., Paerels, F., & Liedahl, D. A. 2001, *ApJ*, 557, L101
- Davies, S. R. 1990, *MNRAS*, 244, 93
- Davis, J. E. 2001, *ApJ*, 562, 575
- Griffiths, R. E., Gursky, H., Schwartz, D. A., et al. 1978, *Nature*, 276, 247
- Heinz, S., & Nowak, M. A. 2001, *MNRAS*, 320, 249
- Iaria, R., Di Salvo, T., Burderi, L., & Robba, N. R. 2001, *ApJ*, 557, 24
- Iaria, R., di Salvo, T., Burderi, L., et al. 2011, *A&A*, 534, A85
- Iaria, R., Di Salvo, T., D’Ai, A., et al. 2013, *A&A*, 549, A33
- Jain, C., Paul, B., & Dutta, A. 2010, *MNRAS*, 409, 755
- Ji, L., Schulz, N. S., Nowak, M. A., & Canizares, C. R. 2011, *ApJ*, 729, 102

- Jonker, P. G., & van der Klis, M. 2001, *ApJ*, 553, L43
- Mason, K. O., Seitzer, P., Tuohy, I. R., et al. 1980, *ApJ*, 242, L109
- Mason, K. O., & Cordova, F. A. 1982, *ApJ*, 255, 603
- Parmar, A. N., Oosterbroek, T., Del Sordo, S., et al. 2000, *A&A*, 356, 175
- Sasano, M., Makishima, K., Sakurai, S., Zhang, Z., & Enoto, T. 2014, *PASJ*, 66, 35
- Seitzer, P., Tuohy, I. R., Mason, K. O., et al. 1979, *IAU Circ.*, 3406, 1
- Verner, D. A., Ferland, G. J., Korista, K. T., & Yakovlev, D. G. 1996, *ApJ*, 465, 487
- White, N. E., Becker, R. H., Boldt, E. A., et al. 1981, *ApJ*, 247, 994
- Wilms, J., Allen, A., & McCray, R. 2000, *ApJ*, 542, 914